

Article

Historical aerial surveys map long-term changes of forest cover and structure in the central Congo Basin

Koen Hufkens^{1,2,*} , Thalès de Haulleville³, Elizabeth Kearsley¹, Kim Jacobsen^{2,3}, Hans Beeckman³, Piet Stoffelen⁴, Filip Vandelook⁴, Sofie Meeus⁴, Michael Amara⁵, Leen Van Hirtum⁵, Jan Van den Bulcke¹, Hans Verbeeck¹, Lisa Wingate²

¹ Ghent University, Ghent, Belgium;

² INRA, UMR ISPA, Villeneuve d'Ornon, France;

³ Royal Museum for Central Africa, Tervuren, Belgium;

⁴ Botanic Garden Meise, Meise, Belgium;

⁵ National Archives of Belgium, Brussels, Belgium;

* Correspondence: koen.hufkens@gmail.com

Academic Editor: name

Version December 23, 2019 submitted to Remote Sens.

1 Abstract: Land Use and Land Cover change (LULCC) of African rainforest contribute to global carbon
2 emissions. Yet, most historical estimates of LULCC and their carbon emissions rely on non-spatially
3 explicity data in the pre-satellite era (< 1972). Past studies have expanded this pre-satellite time
4 frame with declassified satellite surveillance data or aerial surveys, but none cover the Congo Basin.
5 Here, we use historical aerial survey photos to map the extent and structure of LULCC around
6 Yangambi, central Congo Basin, in 1958. Our study leveraged Structure-from-Motion to generate
7 a large orthomosaic covering 828 km², counting 733 million pixels, at a sub meter resolution and
8 geo-referenced to ~4.7 ± 4.3 m. Primary forest in the orthomosaic was classified with a Convoluted
9 Neural Network Deep Learning approach. We used these data to quantify LULCC, landscape
10 and canopy complexity and scale above ground biomass between historical and contemporary
11 condition. We show a shift from historical highly structured industrial deforestation in 1958 (162
12 km²), to contemporary smallholder farming clearing (88 km²), increasing landscape fragmentation
13 and forest edges. Efforts to quantify canopy texture and their link to carbon storage had limited to
14 no success. Our analysis provides an insight in key spatial and temporal patterns of deforestation
15 and reforestation at a multi-decadal scale and provide a historical context to land-cover and land-use
16 change spatial patterns for past and ongoing field research in the area.

17 Keywords: Aerial survey, data recovery, CNN, Deep Learning, SfM, Congo Basin

18 1. Introduction

19 The functioning of a tropical forest, and its capacity to sequester carbon, is heavily influenced
20 by anthropogenic disturbances such as selective logging, clear felling, or slash and burn practices, all
21 increasing forest fragmentation. This increased pace in the loss of rainforest cover [1] is predicted to
22 negatively impact the function of these tropical forests, and their future capacity to sequester carbon,
23 as anthropogenic disturbances such as selective logging, clear felling, or slash and burn practices
24 collectively contribute to increasing forest fragmentation.

25 These forest fragments and their edges contain fewer large trees [2], in part due to their hotter and
26 brighter microclimates [3]. Similarly, species composition and biodiversity [4] are negatively affected.
27 Spatial disturbances also have an explicit temporal component, where the time since disturbance
28 affects the strength of the effects [5]. Deforestation and gap formation also influence the overall canopy
29 structure, where pioneer species grow taller and with narrower crowns [4,6] affecting the forest light
30 regime and carbon dynamics [7]. As such, anthropogenic factors through land-use and land cover
31 change (LULCC) heavily affect forest structure and functioning [5,8,9]. In the tropics the majority of
32 emissions originate from deforestation and forest degradation [10–12] contributing to 10–15% of the
33 total global emissions [13] and concomitant losses in biodiversity losses [14,15] and how LULCC is
34 evolving over time. Although the African rainforest is the second largest on Earth and covers ~630
35 million ha, representing up to 66 Pg of carbon storage [16], and currently loses forest at an increasing
36 pace [1]. Yet, the tropics is now becoming a large source of CO₂ to the atmosphere as deforestation and
37 forest degradation [10–12] contribute up to 10–15% of the total global CO₂ emissions [13]. Furthermore,
38 recent estimates show that 31% of recent carbon emissions are caused by edge effects alone [9]. In
39 this context, there are very few long term forest inventory plots that presently exist in the central
40 Congo Basin [17,18]. This further limits the accuracy of current biomass estimates and challenges
41 our understanding of how forest structure and function changes in the short and long term in these
42 ecosystems [19,20].

43 Historical estimates of LULCC, and their carbon emissions, exist [11,21–23], however they
44 generally rely on non-spatially explicit data in the pre-satellite era (< 1972) [24]. These analysis
45 often use FAO statistics, historical land-use sources, and/or population and socio-economic data [11],
46 as limited earlier spatial data sources are available [10,25]. For example, the Houghton [24] long-term
47 study used FAO and national censuses alongside a bookkeeping model to estimate carbon emissions
48 from LULCC. Other studies use remote sensing data, but are limited in time to recent decades [11,22].
49 These proxy based studies have a limited view on long-term direct and indirect spatial effects of
50 deforestation. As such, both the spatial structure and the fragmentation pattern of a forest combined

51 with its life history has a profound effect on carbon emssions. However, in this context remote
52 sensing assessments provide more accurate spatial information to help estimate carbon emissions [26].

53 Past studies expanded knowledge during the pre-satellite time frame through the use of now
54 declassified satellite surveillance data to map deforestation in the US, central Brazil, and post world war
55 II Germany [27,28]. In some cases these records could extend back in time even further using historical
56 aerial survey images. In northern Europe especially these data are well known and used, for example
57 to map the extent of forest cover across ~100 km² regularly, and at times using automated workflows
58 [29]. Survey data across the African continent is less common or inaccessible or both. Some studies
59 do exist, both Buitenwerf *et al.* [30] and Okeke and Karniel [31] used aerial survey images to map
60 vegetation changes in South African savannas and the Adulam Nature Reserve, respectively. Whilst
61 Frankl *et al.* [32] used 20 aerial survey images to map the Ethiopian highlands of 1935. High resolution
62 aerial or surveillance satellite images provide scientists tools to monitor forest extent and structure over
63 long time frames. Moreover, canopy texture from aerial survey images has been successfully linked
64 to above ground biomass [33–35]. Thus using texture based metrics obtained from (high resolution)
65 remote sensing data opens up possibilities to link historical aerial footage to carbon density across
66 large spatial extents [34].

67 Given the impact of LULCC on the structure and functioning of tropical forests, and their influence
68 on both carbon dynamics [19] and biodiversity [15], accurate long term reporting of historical forest
69 cover in the pre-satellite era is an imperative [36]. In this study we use a combination of historical
70 aerial photography and contemporary remote sensing data to map long-term changes in the extent
71 and structure of the tropical forest surrounding Yangambi, in the central Congo Basin at the beginning
72 of 1958 and the start of the antrophocene [37]. Our analysis provides a historical insight into important
73 LULCC spatial patterns in Yangambi, such as fragmentation and edge complexity. Our analysis further
74 contextualises the influence of changes in the forest's life history on past and current research into
75 Above Ground Carbon (AGC) storage [19] and biodiversity [15] in the central Congo Basin.

76 2. Methods

77 2.1. Historical data acquisition

78 Data for the central Congo Basin region, surrounding Kisangani, were collected in several flights
79 during the dry season of 1958 and 1959 (from 8/01/1958 to 20/02/1958 and from 28/12/1958 to
80 9/01/1959 respectively, see Appendix Figure 1) to generate topographic maps of the area, supervised
81 by the “Institut Géographique du Congo Belge” in Kinshasa (then Léopoldville). Black-and-White
82 infrared images (0.4 - 0.9 μm) were gathered along flight paths running mostly from west to east,
83 between 9 - 11h local time. Along a flight path continuous images were taken using a Wild Heerburgg

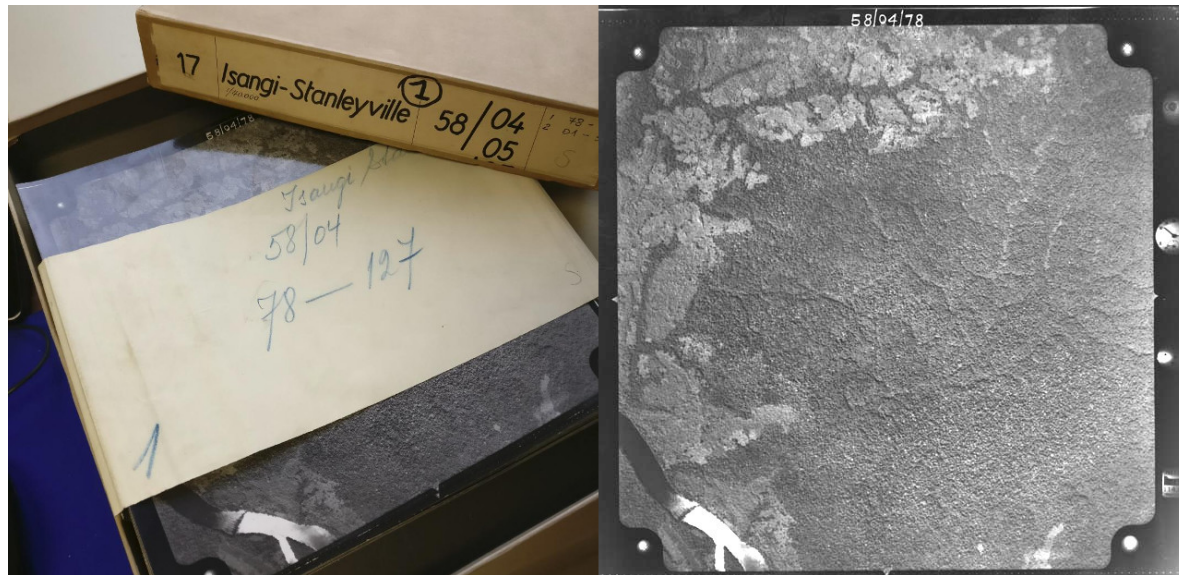


Figure 1. A box of historical aerial photographs (left) and a single aerial photograph (right) showing part of the Congo river. Note the meta-data provided in the margins of the image such as acquisition time and flight height and the solar glare on the Congo river.

84 RC5a (currently Leica Geosystems) with an Aviogon lens assembly (114.83mm / f 5.6, with a 90° view
 85 angle) resulting in square photo negative of 180 by 180 mm. Flights were flown at an average absolute
 86 altitude of ~5200 m above sea level, covering roughly 18 530 km² at an approximate scale of 1/40
 87 000. The use of the integrated autograph system ensured timely acquisition of pictures with a precise
 88 overlap (~1/3) between images. This large overlap between images together with flight parameters
 89 would allow post-processing, using stereographs, to create accurate topographic maps. Original data
 90 from this campaign are stored in the [Royal Museum for Central Africa](#) in Tervuren, Belgium (Figure 1).

91 2.2. Site selection

92 We prioritised flight paths and images that contained current day permanent sampling plots,
 93 larger protected areas, and past agricultural and forest research facilities (Figure 2). This selection
 94 provides a comprehensive mapping of the Yangambi area and the life history of the forest surrounding
 95 it. Thereafter, we selected flight paths 1 through 11 for digitization. From this larger dataset of 334
 96 images we selected 74 survey images for orthomosaic compositing and further analysis. All the
 97 selected images stem from the flight campaign made during January and February of 1958. The area
 98 includes the Yangambi village, 20 contemporary permanent sampling plots [19], past and present
 99 agricultural experimental plots [38] and large sections of the Yangambi **UNESCO Man and Biosphere**
 100 **reserve** surrounding to the west and east of the village. Although not formally mosaicked we provided
 101 a full dataset of pre-processed images using the cropping and normalization routines described below.
 102 The latter data was not used in subsequent LULCC analysis, but has been archived and made available
 103 to the public separately (see code & data availability statement below).

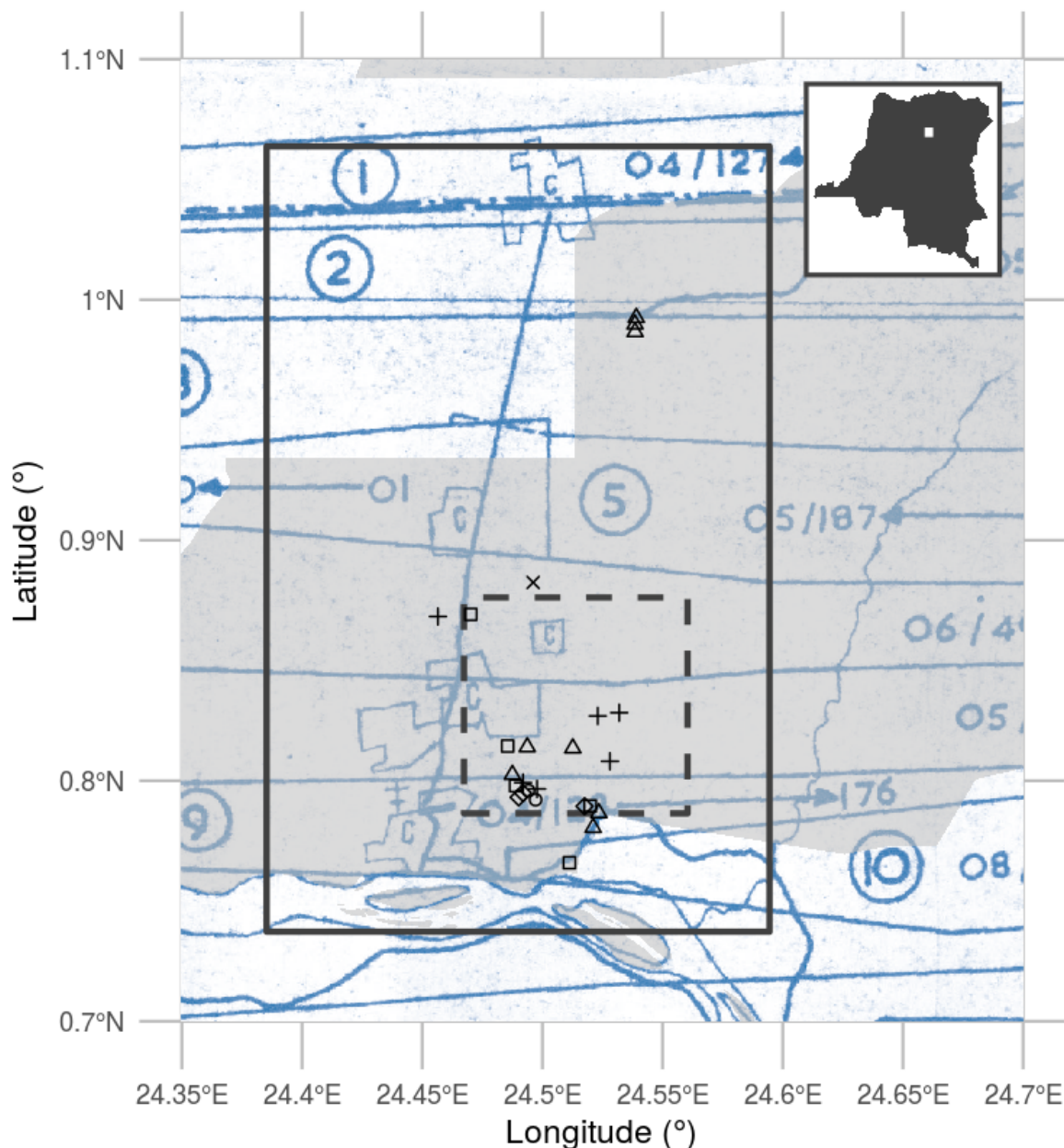


Figure 2. Overview of the historical flight paths during aerial photo acquisition and ancillary data used in this study. The bounding box of the orthomosaic data presented in this study is shown as a rectangle (23x36 km). The outline of a recent high-resolution Geo-eye panchromatic image is shown as a dashed dark grey rectangle (10x10km). The location of various permanent sampling plots are shown as x, +, and open squares and triangles for the mixed, mono-dominant and edge plots respectively. The grey polygon delineates the current day Yangambi Man and Biosphere reserve. The inset, top right, situates the greater Yangambi region with the DR Congo. The full flight plan and details are shown in Appendix Figure 1 and 2

104 2.3. *Digitization and data processing*

105 All selected images, covering the Yangambi area, were contact prints as original negatives of the
106 prints were not available. Images were scanned at a resolution exceeding their original resolution
107 (or grain) at the maximal physical resolution of an Epson A3 flatbed scanner (i.e. 2400 dpi or 160MP
108 per image) and saved as lossless tiff images. Data were normalized using contrast limited histogram
109 equalization [39] with a window size of 32 and a clip limit of 1.5. Fiduciary marks were used to rectify
110 and downsample the images into square 7700x7700 pixel images (~1200 dpi, 81MP). This resulted in a
111 dataset with digital images at a resolution that remained above the visible grain of the photographs,
112 whilst the reduced image size facilitated easier file handling and processing speed.

113 Data was processed into a georeferenced orthomosaic using a Structure from motion (SfM, Ullman
114 [40]) approach implemented in [Agisoft Metashape](#) version 1.5.2 (Agisoft LLC, St. Petersburg, Russia).
115 An orthomosaic corrects remote sensing data to represent a perfectly downward looking image, free
116 from perspective distortions due to topography and camera tilt. Using the SfM technique features,
117 areas in images with a large degree of similarity, are matched across various images to reconstruct
118 a three dimensional scene (topography) from two-dimensional image sequences. During the SfM
119 analysis we masked clouds, glare or large water bodies such as the Congo river.

120 We calculated the orthomosaic using a low resolution point cloud and digital elevation map
121 (DEM). Additional ground control points were provided to assist in the referencing of image and
122 constrain the optimization routine used in the SfM algorithm. Ground control points consisted of
123 rooftop edges of permanent structures which could be verified in both old and new aerial imagery
124 (i.e. ESRI World Imagery). Although clouds were removed during the SfM routine we did not mask all
125 clouds in the final orthomosaic to maximize forest coverage. The final scene was cropped, to provide
126 consistent wall to wall coverage of the reconstructed scene. The orthomosaic was exported as a geotiff
127 for further georeferencing in QGIS [41] using the georeferencer plugin (version 3.1.9) and additional
128 ESRI World Imagery high resolution reference data. We used 3rd degree polynomial and 16 ground
129 control points to correct the final image. Ground control points, raw image data and final processed
130 image are provided in addition to measures of uncertainty such as mean root mean squared (RMSE),
131 mean and median error across all ground control points. All subsequent analysis are executed on the
132 final geo-referenced orthomosaic or subsets of it.

133 2.4. Land-Use and Land-Cover Change

134 2.4.1. Classifying forest cover

135 We automatically delineated all natural forest in the historical data, thus excluding tree plantations,
136 thinned or deteriorated forest stands, fields and buildings. We used the Unet Convolved Neural
137 Net (CNN, Ronneberger *et al.* [42]) architecture implemented in Keras [43] with an efficientnetb3
138 backbone [44] running on TensorFlow [45] to train a binary classifier (i.e. forest or non-forested).
139 This methodology is increasingly being used to automate pixel-level classification in (color) digital
140 photography data [46]. Training data were collected from the orthomosaic by randomly selecting 513
141 pixel square tiles from homogeneous forested or non-forested areas within the historical orthomosaic.
142 Homogeneous tiles were combined in synthetic landscapes using a random gaussian field based binary
143 mask (Figure 3). We generated 5000 synthetic landscapes for training, while 500 landscapes were
144 generated for both the validation and the testing dataset. Source tiles did not repeat across datasets to
145 limit overfitting. In order to limit stitch line misclassifications, along the seams of mosaicked images,
146 we created synthetic landscapes with different forest tiles to mimick forest texture transitions. We
147 applied this technique to 10% of the generated synthetic landscapes. The CNN model was trained
148 for 100 epochs on a graphics processing unit (GPU) maximizing the Intersect-over-Union (IoU) using
149 additional data augmentation. Data augmentation included random cropping to 320 pixel squares,
150 random orientation, scaling, perspective, contrast and brightness shifts and image blurring. During
151 final model evaluation we report the IoU of our out-of-sample test datasets. The optimized model was
152 used to classify the complete orthomosaic using a moving window approach with a step size of 110
153 pixels and a majority vote across overlapping areas to limit segmentation edge effects. We refer to
154 Figure 4 for a synoptic overview of the full deep learning learning workflow.

155 To map long term land-use and land-cover change in the Yangambi region we used the
156 contemporary Global Forest Change version 1.6 data (GFC, tile 10N-020E) [10]. Using this data
157 we calculated the latest state of the forest with respect to the conditions at the start of 1958, 60 years
158 earlier. In our analysis we only included forested pixels which recorded no loss throughout the whole
159 2000 - 2018 period. As the resolution of the historical forest classification exceeds that of the GFC map
160 we downsampled our historical forest cover data to 30m GFC resolution. We masked out all water
161 bodies using the Global Forest Change survey data mask layer, and limited the analysis to the right
162 bank of the Congo river. Where the datasets overlap we provide summary statistics of deforestation,
163 reforestation and afforestation.



Figure 3. An example synthetic landscape, combining homogeneous forest and non-forest images into a patchy landscape using random gaussian field based masks. The left panel shows a combined synthetic landscape, while the right panel shows the corresponding forest (black) and non-forest (white) labels.

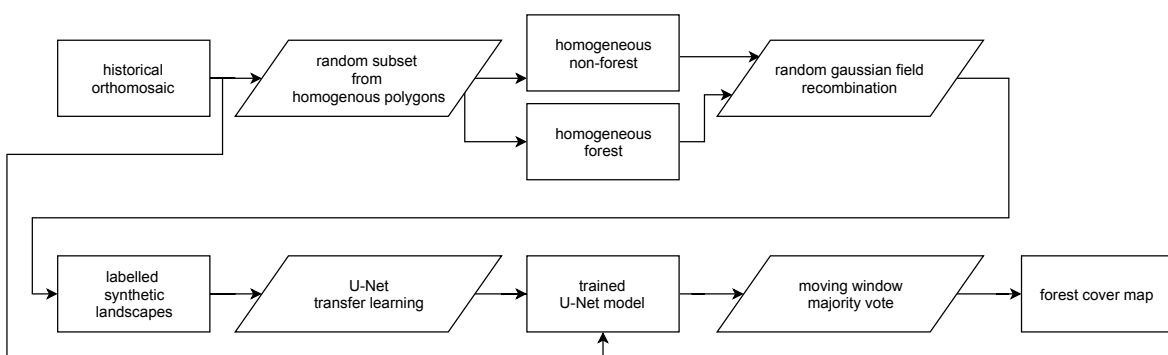


Figure 4. A diagram of the deep learning workflow followed in training a binary forest / non-forest cover convolutional neural net U-Net model to generate our forest cover map.

164 2.4.2. Landscape fragmentation & Above Ground Carbon estimates

165 To quantify changes in the structure of forest cover and its disturbances we used spatial pattern
166 analysis landscape fragmentation metrics [47]. We report the ratio of edge to area and the fractal
167 index to quantify landscape complexity of forest disturbances. Statistics were calculated for all forest
168 disturbance patches larger than 1 ha using the R package landscapemetrics [48]. We provide mean
169 and standard deviation on edge, area, their ratio and fractal dimension for both the historical and
170 contemporary Hansen *et al.* [10] forest cover maps.

171 We estimated above ground carbon (AGC) losses and gains over time using plot based averages
172 of recent inventory data at permanent sampling plots in the area (Figure 2). We refer to Kearsley *et al.*
173 [19] for the survey method and allometric relations used to scale the survey data. Unlike standard
174 square 1 ha plots edge plots were set back 200m from forest edges and were 50x200m, with the 50m
175 side of the plot along the forest edge and continuing 200m into the forest (Appendix Table 1). We
176 further confirmed that forest edge plots did not show a significantly different AGC compared to those
177 of non-edged / mixed forest plots (Mann Whitney U test, $p < 0.05$). Thus it was not necessary to
178 explicitly quantify changes in AGC caused by edge effects. Moreover, we used the mean values of the
179 mixed forest as representative for potential AGC losses. Despite the challenges inherent in quantifying
180 AGC for forest edges we mapped the total extent of the edges in the contemporary landscape. To
181 align our landscape analysis with exploratory analysis of the survey data we used a buffer of 200m to
182 estimate the extent of forest edges and patches, up to the location of forest edge plots.

183 Surveys of old plantations show a large variation in AGC, depending on age and the crop type.
184 For example, the AGC values varied from 168.67 to 86.55 g Mg C ha⁻¹, for *Hevea brasiliensis* (rubber
185 tree) and *Elaeis guineensis* (oil palm) plots respectively (Bustillo *et al.* [49], personal communications).
186 These higher values are in line with the mixed AGC estimates in the area, while the palm plantations
187 resemble old-regrowth values (81.8 Mg C ha⁻¹, see Table A1). We therefore use both the estimates
188 of old-regrowth and mixed forest to estimate AGC for regrowth. We did not have sufficient data to
189 account for individual changes in AGC across plantations.

190 2.5. Canopy structure & FOTO texture analysis

191 We compared the structure of the canopy both visually and using Fourier Transform Textural
192 Ordination (FOTO, Couteron [50]). Fourier Transform Textural Ordination uses a principal component
193 analysis (PCA) on radially averaged 2D Fourier spectra to characterize canopy (image) texture. The
194 FOTO technique was first described by Couteron [50] to quantify canopy stucture in relation to biomass
195 and biodiversity, and can be used across multiple scenes using normalization [35].

196 We used an area of 400x400m (16 ha) around contemporary permanent sampling plot locations
197 to quantify the general state of the canopy in both historical and contemporary remote sensing data.
198 Contemporary data were resampled to the resolution of the historical data using a nearest neighbour
199 interpolation for comparison. We used the first acquisition of a pan-chromatic Geo-Eye 1 stereo pair
200 (GeoEye, 2012, Thornton, Colorado, U.S.A., order 737537, 2011-11-11 8:55h GMT or 9:55h local time).
201 For permanent sampling plot locations in both historical and contemporary data a rectangular buffer
202 of 200m around the centre of all plots was used to create small image subsets. All image subsets were
203 processed using the R based FOTO implementation and package [51] using global normalization,
204 ensuring intercomparability of texture metrics across time and space [35]. We used a FOTO (moving)
205 window size of 187 pixels (or ~150m), as described in Solórzano *et al.* [52] and Barbier *et al.* [35], to
206 ensure that multiple individual canopies could be included in the analysis. A buffer with a radius of
207 50m around the center of all permanent sampling plots was used to determine the average value of
208 the first principle component (PC), explaining the majority of the variance in canopy texture. Where
209 both the Geo-Eye data and the orthomosaic image overlapped we processed the intersecting region to
210 explore a wall-to-wall comparison between past and current canopy texture metrics.

211 We used the standard FOTO methodology with fixed zones, instead of the moving window
212 approach. The window size was set to the same size (187 pixels or ~150m) as used in the moving
213 window analysis above. To account for illumination differences between the two scenes we applied
214 histogram matching. No global normalization was applied, as the scene was processed as a whole. PC
215 values from this analysis for all permanent sampling plots in both image scences were extracted using
216 a buffer with a radius of 50m.

217 For both site based and scene analysis we correlate PC values with permanent sample plot
218 inventory data such as stem density, above ground biomass and tree species richness. Additional
219 comparisons are made between contemporary Geo-Eye data and the historical orthomosaic derived PC
220 values. Due to the few available permanent sampling plots in both scenes we used a non-parametric
221 paired signed rank (Wilcoxon) test to determine differences between the PC values of the Geo-Eye and
222 historical orthomosaic image scenes across mono-dominant and mixed forest types. In all analysis,
223 mono-dominant site 4 was removed from the analysis due to cloud contamination.

224 3. Results

225 Our analysis provides a first spatially explicity historical composite of aerial survey images
226 mapping LULCC within the Congo Basin. The use of high resolution historical images combined with
227 structure from motion image processing techniques allowed us to mosaic old imagery across a large
228 extent. The final orthomosaic composition of the Yangambi region resulted in an image scene covering

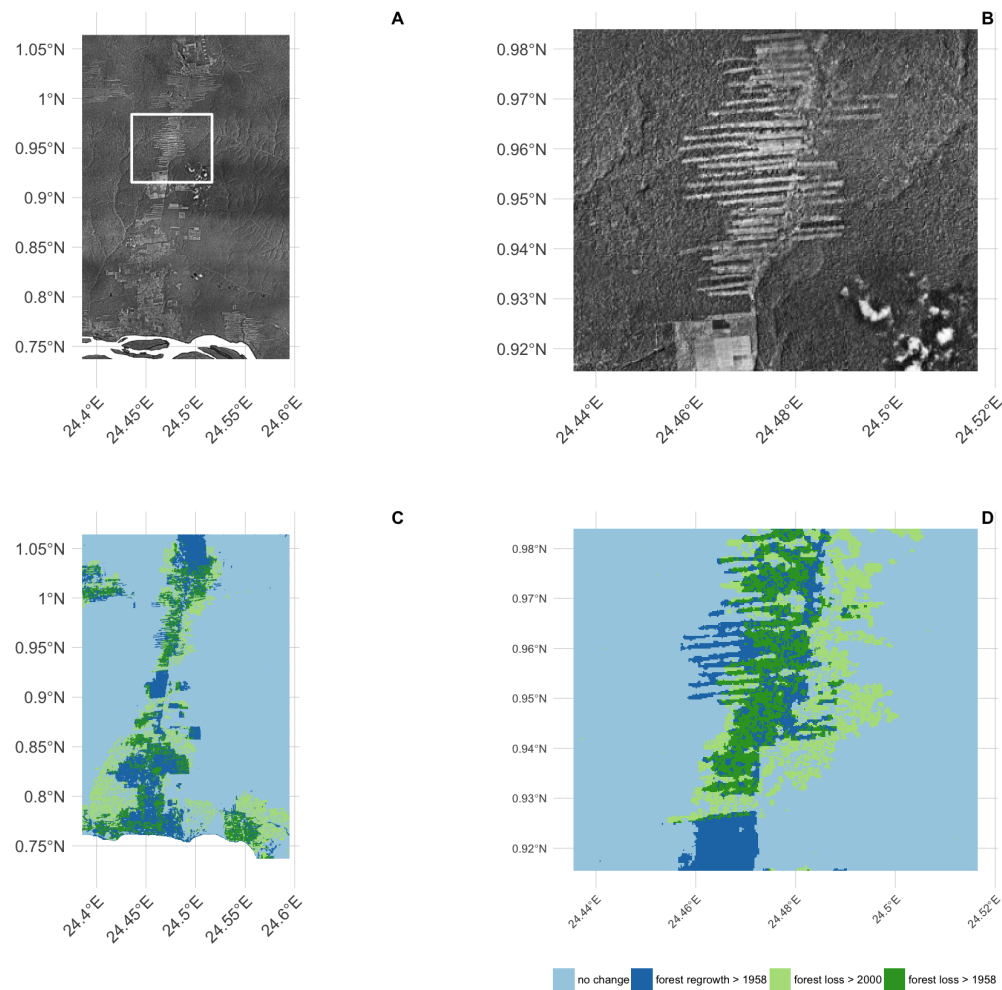


Figure 5. Overview of the final orthomosaic of the greater Yangambi region (A), a detailed inset (B) and the derived land use land cover change map displayed as the difference between a manual classification of the orthomosaic and a recent map by Hansen et al. 2013 (C) and the corresponding land cover map for inset B (D).

approximately 733 million pixels across $\sim 828 \text{ km}^2$ ($\sim 23 \times 36 \text{ km}$, Figure 2). The overall accuracy of the structure from motion orthomosaic composition was 0.88 m/pixel using the sparse cloud DEM for corrections at 45.8 m/pixel. The resulting georeferenced scene had a spatial accuracy of approximately 23m. Further georeferencing outside the SfM workflow reduced the mean error at the ground control points to $5.3 \pm 4.9 \text{ px}$ ($\sim 4.7 \pm 4.3 \text{ m}$), with a median error of 2.9 px (2.6m). The orthomosaic served as input for all subsequent LULCC analysis with all derived maps provided with the manuscript repository (see data & code availability statements below).

3.1. Land-use and Land-Cover Change & Above Ground Carbon

Our CNN deep learning classifier reached an Intersection-over-Union (IoU) accuracy of 97% on the detection of disturbed forest in out-of-sample test data. Scaling our classifier to the whole historical orthomosaic we detected 162 km^2 (or $\sim 20\%$ of the scene) of disturbed forests. A large fraction of the

²⁴⁰ disturbed area was restored in the period between the two acquisitions. In total, 99 km², or little over
²⁴¹ half of the affected forest was restored (Figure 5C-D, dark blue). Recent deforested areas, as registered
²⁴² through satellite remote sensing, approximate 88 km² (Table 1, Figure 5C-D / light green).

²⁴³ Recent deforestation follows a distinctly different pattern compared to historical patterns.
²⁴⁴ Historical deforestation showed a classical fishbone pattern for forest clearing with very sharp edges,
²⁴⁵ while current patterns are patchy and ad-hoc (figure 5D, dark blue and green colours respectively).
²⁴⁶ These differences are reflected in the analysis of landscape metrics of forest loss. Between the historical
²⁴⁷ and contemporary LULCC maps we see an increase in small disturbances, as indicated by the
²⁴⁸ decreasing area of the mean patch size, down to 37 ha from 120 ha historically, while perimeter
²⁴⁹ lengths remained approximately the same, with 8653m and 9902m for historical and contemporary
²⁵⁰ maps respectively (Table 2). This shift in perimeter area ratio led to a similar change in the fractal
²⁵¹ index, increasing in value to 1.13 ± 0.07 from 1.10 ± 0.05 over time. Values closer to a fractal index of 2
²⁵² suggest a more complex (fragmented) landscape.

²⁵³ A comparison of forest edge plots with mixed forest plots showed no significant difference in
²⁵⁴ AGC, or other reported values such as species richness, basal area or stem density (Mann Whitney U
²⁵⁵ test, $p < 0.05$). Edge influence did not extend beyond 200 m from a forest edge, but still represented an
²⁵⁶ area of 132 km².

²⁵⁷ Changes in both land-use and land-cover led to concomitant changes in above ground carbon
²⁵⁸ stocks. Recovery throughout the region was characterized for patches of forest and plantations.
²⁵⁹ Assuming high density stands, based on previous work, this could amount to a carbon gains of 1592
²⁶⁰ Gg C, offsetting more recent losses of approximately 1408 Gg C. On the other hand, at the low end, if
²⁶¹ we assume a lower carbon density of 81.8 Mg C ha⁻¹ this would result in a total carbon gain of 811 Gg
²⁶² C. Using our approach results indicate that overall deforestation around Yangambi has resulted in a
²⁶³ loss of ~2416 Gg C in AGC stocks.

Table 1. Land use land cover change statistics of forest cover around Yangambi in the central Congo Basin. The data evaluates a difference between a historical (1958) aerial photography based survey and the Hansen et al. 2013 based satellite remote sensing data. Spatial coverage statistics are provided in square kilometers (km) and hectares (ha), rounded to the nearest integer as well as Above Ground Carbon (AGC) scaled using recent survey measurements.

	km ²	ha	AGC (Gg C ha ⁻¹)
Forest	685	68455	-
- of which edges	132	13151	-
Regrowth > 1958 loss	99	9918	811 - 1592
Loss > 2000	88	8776	1408
Loss > 1958 (permanent)	63	6282	1008

Table 2. Landscape metrics for historical and contemporary deforestation patterns. We report patch perimeter and area, their ratio and fractal dimension. Values are reported as mean \pm standard deviation, across all deforestation patches.

	perimeter (m)	area (ha)	ratio (m^{-1})	fractal dimension
historical	8653 ± 35676	120 ± 659	0.031 ± 0.014	1.099 ± 0.052
contemporary	9902 ± 56975	37 ± 226	0.046 ± 0.014	1.13 ± 0.071

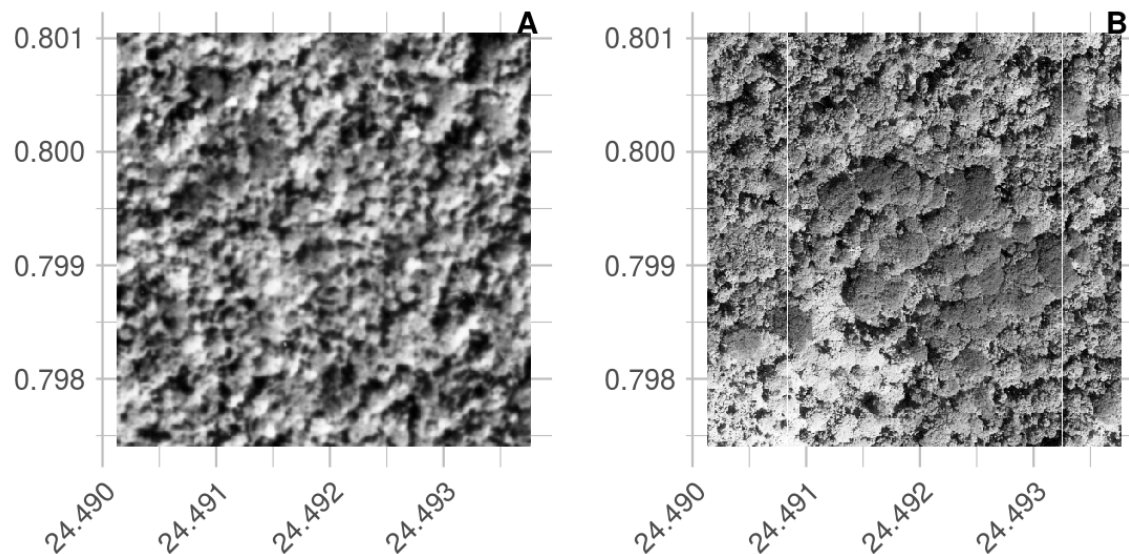


Figure 6. Visual comparison between a historical (A) and contemporary (B) permanent sampling plot. The site is currently listed as a mono-dominant *Brachystegia laurentii* stand. Note the structural differences with a 'coarser' canopy structure in the historical image compared to the more closed contemporary stand.

264 3.2. Canopy structure & FOTO texture analysis

265 Visual interpretation of the scenes provide evidence that most locations do not change dramatically
 266 with respect to canopy composition, except for the large areas of disturbances in contemporary fallow
 267 or young-regrowth plots. One marked difference is noted in the mono-dominant site 6 (Appendix
 268 Table 1). Here, the current mono-dominant *Brachystegia laurentii* is a recent development, changing the
 269 canopy structure visibly during the last half century (Figure 6). The previous varied canopy structure
 270 gave way to a more dense and uniform canopy. This is reflected in a change of the FOTO PC value from
 271 0.19 historically to its current value of 0.54. This historical value is similar to the mean of contemporary
 272 mono-dominant stands with PC averaging 0.34 ± 0.1 , and is only slightly higher than historical values
 273 for a mixed forest (0.18 ± 0.08). The reverse pattern is seen in the contemporary PC values. Here, the
 274 value of 0.54 exceeds those of most mono-dominant stands (0.35 ± 0.08), and is even further removed
 275 from the values noted for mixed forests (0.12 ± 0.03).

276 Using only small subsets around existing permanent sampling plots we show distinct differences
 277 between forest types, with PC values in both historical and contemporary imagery markedly higher

for the mono-dominant forest types compared to all others (Appendix Figure 3). Provided that the young-regrowth and fallow permanent sampling plots have seen recent disturbance the Wilcoxon signed rank test on the mixed and mono-dominant plots between the historical and contemporary PC values did not show a significant difference ($p > 0.05$). Similarly, no significant difference using PC values extracted from the whole scene analysis was noted ($p > 0.05$). Any relationships between contemporary Geo-Eye data and permanent sampling plot measurements of Above Ground Biomass, stem density and species richness were non-significant ($p > 0.05$, Appendix Figures 4-6).

Furthermore, visual inspection of the scene wide analysis suggests historical scenes do not show landscape wide canopy features (Figure 7 A-B), unlike the contemporary scene (Figure 7 C-D). Where the FOTO algorithm picks up landscape features such as changes in texture across the contemporary Geo-Eye scene (e.g. the river valley as a diagonal line in Figure 7D), however, no corresponding landscape patterns are found by the FOTO algorithm in the historical orthomosaic.

4. Discussion

Finely grained spatial data sources, such as remote sensing imagery, are rare before the satellite era (<1970). This lack of data limits our understanding of how forest structure has varied over longer time periods in especially remote areas. Long term assessment can be extended by using large inventories of historical aerial survey data [27,28,53]. However, across the Congo Basin this data is rare, or difficult to access. Despite the difficulties in assessing hidden disturbances caused by deforestation, poorly recorded official assessments or simply those invisible to standard remote sensing techniques [6], remote sensing generally remains the best way to map and quantify LULCC [11]. Despite these challenges in recovery and validation we present a first analysis of LULCC using historical aerial survey data for the central Congo Basin. We used a combination of Structure-from-Motion and a convolutional neural net deep learning approach to map deforestation across a large extent, providing a long term view of LULCC in the central Congo Basin

4.1. Data recovery challenges

In our study the archive data recovered was limited to contact prints and therefore did not represent the true resolution of the original negative. In addition, analogue photography clearly produces a distinct softness compared to digital imagery (Figure 4). Despite favourable nadir image acquisitions [54] image softness combined with illumination effects between flight paths, and the self-similar nature of vast canopy expanses [55–57], limited our ability to provide wall-to-wall coverage of the entire dataset containing 334 images. Few man made features in the scenes also made georeferencing challenging. Although the village of Yangambi provided a range of buildings as (hard-edge) references, other areas within the central Congo Basin might have fewer permanent

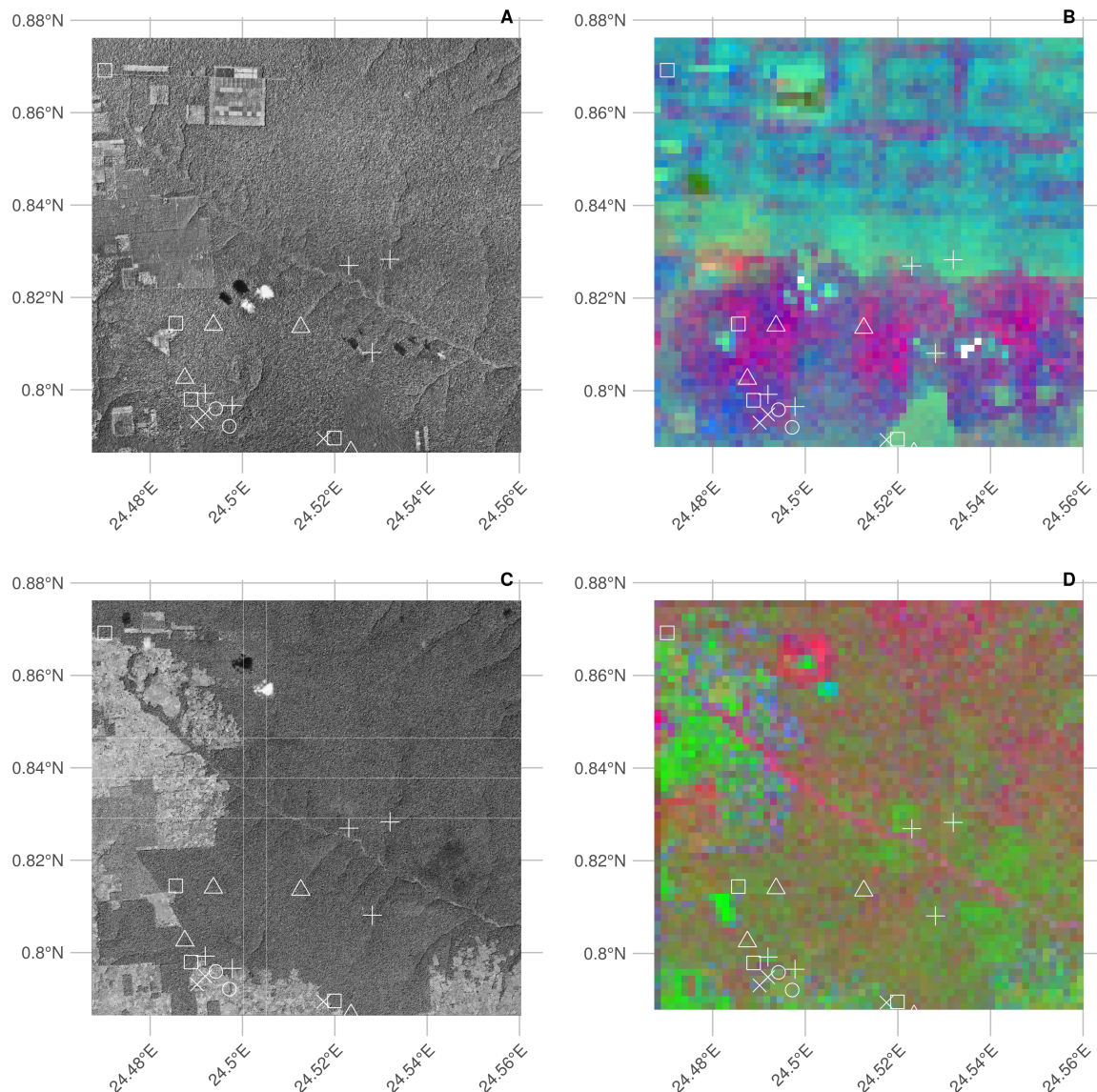


Figure 7. RGB visualizations of the first three principal components of scene wide FOTO texture analysis of historical and current (Geo-Eye) imagery. Current permanent sampling plots of mono-dominant, mixed, fallow and young (edge) forest plots are marked with open triangles, open circles, open squares and crosses, respectively.

311 structures and would require the use of soft-edged landscape features (e.g. trees, river outflows).
312 Research has shown that soft-edged features can help georeference scenes even when containing
313 few man-made features [58], however accuracy becomes compromised. Our two step georeferencing
314 approach resulted in a referencing accuracy of $\sim 4.7 \pm 4.3$ m across reference points. However, it should
315 be noted that referencing accuracy of the final scene is less constrained toward the edges of the scene.

316 *4.2. Land-use, Land-Cover change & Above Ground Carbon*

317 When classifying our orthomosaic into forest and non-forest states we favoured a deep learning
318 supervised classification using a Convolved Neural Network over manual segmentation to guarantee
319 an “apples-to-apples” comparison between the historical and the contemporary GFC forest cover
320 maps. We acknowledge that both classifications use different features, i.e. spectral or spatial data, but
321 attain a similarly high accuracy of 97% and 99% [10], for the GFC and our CNN map respectively.
322 Despite a number of challenges we were able to map and quantify a vast continuous area of tropical
323 forest, with limited manual annotation requirements.

324 Our analysis shows that the majority of deforestation around Yangambi happened toward the late
325 1950’s (162 km^2). Considerable regrowth has occurred since the aerial survey was executed (99 km^2),
326 and socio-economic instability prevented further large scale forest exploitation. In particular, many
327 plantations have reached maturity and forest has re-established in previously cleared or disturbed
328 areas. The majority of this forest recovery takes the form of isolated patches of forest but is offset
329 by further deforestation of previously untouched forest. Generally, the function and structure of
330 forests can be influenced by forest edges that are located up to 1km away however most effects are
331 pronounced within the first 300m from the edge [59]. Our analysis of edge effects on AGC has shown
332 that the influence is negligible 200m away from the edge. Phillips *et al.* [60] have shown similar weak
333 responses to edge effects in the Amazon forest. Due to a lack of data on the extent (depth) of edge
334 effects and their influence on AGC beyond 200m we did not include any estimates of carbon loss
335 or gain within these zones. However, it must be stated that the influence of edges throughout the
336 landscape was not marginal. as these areas would account for 132 km^2 . Thus edges could have a
337 substantial negative [9] or positive [61] influence on AGC. Similarly, uncertainties in how to explicitly
338 correct for plantations in the landscape present a further challenge. Thus although our estimates
339 are only indicative they do underscore the important influence of landscape structure when carbon
340 accounting. However, our findings do not indicate that deforestation in Congo basin is declining, on
341 the contrary.

342 Over the past half century there has been a clear shift in land use in Yangambi (Figure 5). Land
343 use has shifted away from for example a regular fishbone deforestation pattern that emerges when

344 (large scale) agricultural interests dominate the landscape [62], to a more fragmented landscape
345 (Figure 5D). The latter former? is consistent with historical land management at the time of the aerial
346 survey [49]. These regular patterns have since been reversed because of a decrease in large scale
347 intensive agriculture, replaced by ad-hoc small scale subsistence farming with large perimeter to area
348 relationships (i.e. ragged edges). Consequently, edge effects in the current landscape are far more
349 pronounced than in the historical scene.

350 Visual inspection of the images also suggests that reforestation within the historically cleared areas
351 and experimental plots is not necessarily limited to areas far removed from more densely populated
352 areas. For example, large reforested areas exist close to the Congo stream and Yangambi village itself
353 (Fig. 5). Here, regional political components, such as land leases and large scale ownership could
354 have played a role in safeguarding some of these areas for rewilding or sustainable management
355 [63,64]. Despite widespread anthropogenic influences throughout the tropics [37] the retention of
356 these forested areas show the potential of explicit or implicit protective policy measures (e.g. INERA
357 concessions, Bustillo *et al.* [49]) on a multi-decadal time scale. Forest regrowth in non-continuous areas
358 within Yangambi could increase landscape connectivity and help increase biodiversity [15].

359 Our analysis therefore provides an opportunity to highlight and study those regions that have
360 previously suffered confirmed long-term disturbances, and those that have been restored since.
361 Assessments of old plantations and recovering clear-cut forests can serve as a guide to help estimate
362 carbon storage capacity and forest recovery rates in managed and unmanaged conditions [23,25,65]
363 over the mid- to long-term, in support of rewilding and general forest restoration [15,63,64]. In addition,
364 mapping long-term edge effects can further support research into issues such as receding forest edges
365 [59].

366 4.3. Canopy structure & FOTO texture analysis

367 Finally the FOTO technique used to quantify relationships between canopy structure and forest
368 characteristics rendered no valuable insights of either the historical orthomosaic or recent Geo-Eye
369 scene. Similarly weak correlations were found previously by Solórzano *et al.* [52]. In contrast site
370 based texture metric statistics did show correspondence between historical and contemporary satellite
371 imagery. However, none of them were either consistent or significant. Although visual interpretation
372 shows distinctly different canopy structures (Figure 5) the differences in how resolution is defined
373 and issues related to image quality prevented us from quantifying these further. Unlike large scale
374 studies by Ploton *et al.* [33] we could not scale this technique to historical data. We advise that future
375 valorisation efforts should preferentially work from foto negatives (if available) to ensure optimal data
376 quality in resolution, contrast and overall sharpness.

377 5. Conclusion

378 Given the impact of tropical forest disturbances on atmospheric CO₂ emissions, biodiversity and
379 ecosystem productivity accurate long term reporting on land-cover and land-use change especially
380 in the pre-satellite era is an imperative. Our analysis of historical aerial survey images of the Central
381 Congo Basin provides a window into the state of the forest at the start of the anthropocene. Efforts to
382 quantify canopy texture and their link to carbon storage had limited to no success. We have shown that
383 historical aerial survey data can be used to quantify land-use and land-cover change using a highly
384 automated workflow to quantify the structure and extent of forest cover change that can help assess
385 the impact of fragmentation on above ground carbon stocks. We also show a shift from previously
386 highly structured industrial deforestation of large areas, to discrete smallholder clearing for farming,
387 increasing landscape fragmentation but also opportunity for substantial regrowth. Efforts to quantify
388 canopy texture and their link to carbon storage had limited to no success. As such, our analysis
389 provides insights into the state of rarely studied tropical forests and the rate at which deforestation
390 and reforestation has taken place over a multi-decadal scale in the central Congo basin providing a
391 useful historical context to land-cover and land-use change spatial patterns for interpreting past and
392 ongoing field research in the area.

393 6. Additional Information and Declarations

394 6.1. Data availability

395 Hufkens et al. (2019). A curated dataset of aerial survey images over the central Congo Basin,
396 1958. Zenodo: doi.org/10.5281/zenodo.3547767. All data not included in the latter repository can be
397 found bundled with the analysis code as listed below. Proprietary datasets (i.e. Geo-Eye data) are not
398 shared, but purchase order numbers allow for acquisition of these datasets to ensure reproducibility.
399 The Hansen *et al.* [10] image data is freely available from [the GFC project website](#).

400 6.2. Code availability

401 All analysis code is available as an R [66] project (<https://github.com/khufkens/orthodrc>). The
402 analysis relied heavily on the ‘raster’ [67], ‘RStoolbox’ [68], and ‘landscapemetrics’ [48] packages, while
403 post-processing and plotting was facilitated by the ‘tidyverse’ ecosystem [69], ‘ggthemes’ [70], ‘scales’
404 [71] and ‘cowplot’ [72]. Additional plotting elements were formatted or provided by ‘sf’ [73] and
405 ‘rnatural-earth’ [74] packages, respectively. I’m grateful for the contributions to the scientific community
406 by the developers of these packages.

407 **Acknowledgments:** This research was supported through the Belgian Science Policy office COBECORE
408 project (BELSPO; grant BR/175/A3/COBECORE). KH acknowledges funding from the European Union Marie

409 Skłodowska-Curie Action (project number 797668). I'm grateful for the support of Thales D'Haulleville
410 volunteering his time in scanning the images.

411 **Author Contributions:** K.H. conceived and designed the study, analyzed the data, prepared figures and tables,
412 authored, reviewed and approved the final draft of the manuscript. T.d.H. scanned all image data. E.K. and T.d.H.
413 provided plot based AGC estimates. T.D., K.J., E.K., H.B., P.S., F.V.S.M., M.A., J.V.D.B., H.V and L.W. reviewed the
414 final manuscript.

415 **Conflicts of Interest:** The authors declare no conflict of interest. The founding sponsors had no role in the design
416 of the study; in the collection, analyses, or interpretation of data; in the writing of the manuscript, and in the
417 decision to publish the results.

418 References

- 419 1. Butsic, V.; Baumann, M.; Shortland, A.; Walker, S.; Kuemmerle, T. Conservation and conflict in the
420 Democratic Republic of Congo: The impacts of warfare, mining, and protected areas on deforestation.
421 *Biological Conservation* **2015**, *191*, 266–273. doi:10.1016/j.biocon.2015.06.037.
- 422 2. Laurance, W.F.; Delamônica, P.; Laurance, S.G.; Vasconcelos, H.L.; Lovejoy, T.E. Rainforest fragmentation
423 kills big trees. *Nature* **2000**, *404*, 836–836. doi:10.1038/35009032.
- 424 3. Magnago, L.F.S.; Magrach, A.; Laurance, W.F.; Martins, S.V.; Meira-Neto, J.A.A.; Simonelli, M.; Edwards,
425 D.P. Would protecting tropical forest fragments provide carbon and biodiversity cobenefits under REDD+?
426 *Global Change Biology* **2015**, *21*, 3455–3468. doi:10.1111/gcb.12937.
- 427 4. Poorter, L.; Bongers, F. Leaf traits are good predictors of plant performance across 53 rain forest species.
428 *Ecology* **2006**, *87*, 1733–1743. doi:10.1890/0012-9658(2006)87[1733:LTAGPO]2.0.CO;2.
- 429 5. Didham, R.K. Edge Structure Determines the Magnitude of Changes in Microclimate and Vegetation
430 Structure in Tropical Forest Fragments. *Biotropica* **1999**, *31*, 17–30.
- 431 6. Peres, C.A.; Barlow, J.; Laurance, W.F. Detecting anthropogenic disturbance in tropical forests. *Trends in
432 Ecology & Evolution* **2006**, *21*, 227–229. doi:10.1016/j.tree.2006.03.007.
- 433 7. Stark, S.C.; Leitold, V.; Wu, J.L.; Hunter, M.O.; de Castilho, C.V.; Costa, F.R.C.; McMahon, S.M.; Parker,
434 G.G.; Shimabukuro, M.T.; Lefsky, M.A.; Keller, M.; Alves, L.F.; Schietti, J.; Shimabukuro, Y.E.; Brandão,
435 D.O.; Woodcock, T.K.; Higuchi, N.; de Camargo, P.B.; de Oliveira, R.C.; Saleska, S.R. Amazon forest
436 carbon dynamics predicted by profiles of canopy leaf area and light environment. *Ecology Letters* **2012**,
437 *15*, 1406–1414. doi:10.1111/j.1461-0248.2012.01864.x.
- 438 8. Fauset, S.; Gloor, M.U.; Aidar, M.P.M.; Freitas, H.C.; Fyllas, N.M.; Marabesi, M.A.; Rochelle, A.L.C.;
439 Shenkin, A.; Vieira, S.A.; Joly, C.A. Tropical forest light regimes in a human-modified landscape. *Ecosphere*
440 **2017**, *8*, e02002. doi:10.1002/ecs2.2002.
- 441 9. Brinck, K.; Fischer, R.; Groeneveld, J.; Lehmann, S.; Dantas De Paula, M.; Pütz, S.; Sexton, J.O.; Song, D.;
442 Huth, A. High resolution analysis of tropical forest fragmentation and its impact on the global carbon
443 cycle. *Nature Communications* **2017**, *8*. doi:10.1038/ncomms14855.
- 444 10. Hansen, M.C.; Potapov, P.V.; Moore, R.; Hancher, M.; Turubanova, S.A.; Tyukavina, A.; Thau, D.; Stehman,
445 S.V.; Goetz, S.J.; Loveland, T.R.; Kommareddy, A.; Egorov, A.; Chini, L.; Justice, C.O.; Townshend,
446 J.R.G. High-Resolution Global Maps of 21st-Century Forest Cover Change. *Science* **2013**, *342*, 850–853.
447 doi:10.1126/science.1244693.
- 448 11. Houghton, R.A.; House, J.I.; Pongratz, J.; van der Werf, G.R.; DeFries, R.S.; Hansen, M.C.; Le Quéré, C.;
449 Ramankutty, N. Carbon emissions from land use and land-cover change. *Biogeosciences* **2012**, *9*, 5125–5142.
450 doi:10.5194/bg-9-5125-2012.
- 451 12. Tyukavina, A.; Baccini, A.; Hansen, M.C.; Potapov, P.V.; Stehman, S.V.; Houghton, R.A.; Krylov, A.M.;
452 Turubanova, S.; Goetz, S.J. Aboveground carbon loss in natural and managed tropical forests from 2000 to
453 2012. *Environmental Research Letters* **2015**, *10*, 074002. doi:10.1088/1748-9326/10/7/074002.
- 454 13. van der Werf, G.R.; Morton, D.C.; DeFries, R.S.; Olivier, J.G.J.; Kasibhatla, P.S.; Jackson, R.B.; Collatz, G.J.;
455 Randerson, J.T. CO₂ emissions from forest loss. *Nature Geoscience* **2009**, *2*, 737–738. doi:10.1038/ngeo671.
- 456 14. Barlow, J.; Lennox, G.D.; Ferreira, J.; Berenguer, E.; Lees, A.C.; Nally, R.M.; Thomson, J.R.; Ferraz, S.F.D.B.;
457 Louzada, J.; Oliveira, V.H.F.; Parry, L.; Ribeiro de Castro Solar, R.; Vieira, I.C.G.; Aragão, L.E.O.C.; Begotti,

- 458 R.A.; Braga, R.F.; Cardoso, T.M.; Jr, R.C.d.O.; Souza Jr, C.M.; Moura, N.G.; Nunes, S.S.; Siqueira, J.V.;
459 Pardini, R.; Silveira, J.M.; Vaz-de Mello, F.Z.; Veiga, R.C.S.; Venturieri, A.; Gardner, T.A. Anthropogenic
460 disturbance in tropical forests can double biodiversity loss from deforestation. *Nature* **2016**, *535*, 144–147.
461 doi:10.1038/nature18326.
- 462 15. Van de Perre, F.; Willig, M.R.; Presley, S.J.; Bapeamoni Andemwana, F.; Beeckman, H.; Boeckx, P.; Cooleman,
463 S.; de Haan, M.; De Kesel, A.; Dessein, S.; Grootaert, P.; Huygens, D.; Janssens, S.B.; Kearsley, E.; Kabeya,
464 P.M.; Leponce, M.; Van den Broeck, D.; Verbeeck, H.; Würsten, B.; Leirs, H.; Verheyen, E. Reconciling
465 biodiversity and carbon stock conservation in an Afrotropical forest landscape. *Science Advances* **2018**,
466 *4*, eaar6603. doi:10.1126/sciadv.aar6603.
- 467 16. Lewis, S.L.; Lopez-Gonzalez, G.; Sonké, B.; Affum-Baffoe, K.; Baker, T.R.; Ojo, L.O.; Phillips, O.L.; Reitsma,
468 J.M.; White, L.; Comiskey, J.A.; Djuiouo K, M.N.; Ewango, C.E.N.; Feldpausch, T.R.; Hamilton, A.C.;
469 Gloor, M.; Hart, T.; Hladik, A.; Lloyd, J.; Lovett, J.C.; Makana, J.R.; Malhi, Y.; Mbago, F.M.; Ndangalasi,
470 H.J.; Peacock, J.; Peh, K.S.H.; Sheil, D.; Sunderland, T.; Swaine, M.D.; Taplin, J.; Taylor, D.; Thomas, S.C.;
471 Votere, R.; Wöll, H. Increasing carbon storage in intact African tropical forests. *Nature* **2009**, *457*, 1003–1006.
472 Publisher: Earth and Biosphere Institute, School of Geography, University of Leeds, Leeds LS2 9JT, UK.
473 s.l.lewis@leeds.ac.uk.
- 474 17. Verbeeck, H.; Boeckx, P.; Steppe, K. Tropical forests: include Congo basin. *Nature* **2011**, *479*, 179–179.
- 475 18. Lewis, S.L.; Sonke, B.; Sunderland, T.; Begne, S.K.; Lopez-Gonzalez, G.; van der Heijden, G.M.F.; Phillips,
476 O.L.; Affum-Baffoe, K.; Baker, T.R.; Banin, L.; Bastin, J.F.; Beeckman, H.; Boeckx, P.; Bogaert, J.; De Canniere,
477 C.; Chezeaux, E.; Clark, C.J.; Collins, M.; Djagbletey, G.; Djuiouo, M.N.K.; Droissart, V.; Doucet, J.L.;
478 Ewango, C.E.N.; Fauset, S.; Feldpausch, T.R.; Foli, E.G.; Gillet, J.F.; Hamilton, A.C.; Harris, D.J.; Hart, T.B.;
479 de Haulleville, T.; Hladik, A.; Hufkens, K.; Huygens, D.; Jeanmart, P.; Jeffery, K.J.; Kearsley, E.; Leal, M.E.;
480 Lloyd, J.; Lovett, J.C.; Makana, J.R.; Malhi, Y.; Marshall, A.R.; Ojo, L.; Peh, K.S.H.; Pickavance, G.; Poulsen,
481 J.R.; Reitsma, J.M.; Sheil, D.; Simo, M.; Steppe, K.; Taedoumg, H.E.; Talbot, J.; Taplin, J.R.D.; Taylor, D.;
482 Thomas, S.C.; Toirambe, B.; Verbeeck, H.; Vleminckx, J.; White, L.J.T.; Willcock, S.; Woell, H.; Zemagho, L.
483 Above-ground biomass and structure of 260 African tropical forests. *Philosophical Transactions of the Royal
484 Society B: Biological Sciences* **2013**, *368*, 20120295–20120295. doi:10.1098/rstb.2012.0295.
- 485 19. Kearsley, E.; de Haulleville, T.; Hufkens, K.; Kidimbu, A.; Toirambe, B.; Baert, G.; Huygens, D.; Kebede,
486 Y.; Defourny, P.; Bogaert, J.; Beeckman, H.; Steppe, K.; Boeckx, P.; Verbeeck, H. Conventional tree
487 height-diameter relationships significantly overestimate aboveground carbon stocks in the Central Congo
488 Basin. *Nature communications* **2013**, *4*, 2269. doi:10.1038/ncomms3269.
- 489 20. Doetterl, S.; Kearsley, E.; Bauters, M.; Hufkens, K.; Lisingo, J.; Baert, G.; Verbeeck, H.; Boeckx, P.
490 Aboveground vs. Belowground Carbon Stocks in African Tropical Lowland Rainforest: Drivers and
491 Implications. *Plos One* **2015**, *10*, e0143209. doi:10.1371/journal.pone.0143209.
- 492 21. Ramankutty, N.; Foley, J.A. Estimating historical changes in global land cover: Croplands from 1700 to
493 1992. *Global Biogeochemical Cycles* **1999**, *13*, 997–1027. doi:10.1029/1999GB900046.
- 494 22. DeFries, R.S.; Houghton, R.A.; Hansen, M.C.; Field, C.B.; Skole, D.; Townshend, J. Carbon emissions from
495 tropical deforestation and regrowth based on satellite observations for the 1980s and 1990s. *Proceedings of
496 the National Academy of Sciences* **2002**, *99*, 14256–14261. doi:10.1073/pnas.182560099.
- 497 23. Sader, S.A.; Joyce, A.T. Deforestation Rates and Trends in Costa Rica, 1940 to 1983. *Biotropica* **1988**, *20*, 11.
498 doi:10.2307/2388421.
- 499 24. Houghton, R. How well do we know the flux of CO₂ from land-use change? *Tellus B: Chemical and Physical
500 Meteorology* **2010**, *62*, 337–351. doi:10.1111/j.1600-0889.2010.00473.x.
- 501 25. Achard, F.; Beuchle, R.; Mayaux, P.; Stibig, H.J.; Bodart, C.; Brink, A.; Carboni, S.; Desclée, B.; Donnay, F.;
502 Eva, H.D.; Lupi, A.; Raši, R.; Seliger, R.; Simonetti, D. Determination of tropical deforestation rates and
503 related carbon losses from 1990 to 2010. *Global Change Biology* **2014**, *20*, 2540–2554. doi:10.1111/gcb.12605.
- 504 26. Mitchard, E.T.A. The tropical forest carbon cycle and climate change. *Nature* **2018**, *559*, 527–534.
505 doi:10.1038/s41586-018-0300-2.
- 506 27. Song, D.X.; Huang, C.; Sexton, J.O.; Channan, S.; Feng, M.; Townshend, J.R. Use of Landsat and
507 Corona data for mapping forest cover change from the mid-1960s to 2000s: Case studies from the Eastern
508 United States and Central Brazil. *ISPRS Journal of Photogrammetry and Remote Sensing* **2015**, *103*, 81–92.
509 doi:10.1016/j.isprsjprs.2014.09.005.

- 510 28. Nita, M.D.; Munteanu, C.; Gutman, G.; Abrudan, I.V.; Radeloff, V.C. Widespread forest cutting in the
511 aftermath of World War II captured by broad-scale historical Corona spy satellite photography. *Remote*
512 *Sensing of Environment* **2018**, *204*, 322–332. doi:10.1016/j.rse.2017.10.021.
- 513 29. Giordano, S.; Le Bris, A.; Mallet, C. Toward automatic georeferencing of archival aerial photogrammetric
514 surveys. *ISPRS Annals of Photogrammetry, Remote Sensing and Spatial Information Sciences* **2018**, *IV-2*, 105–112.
515 doi:10.5194/isprs-annals-IV-2-105-2018.
- 516 30. Buitenhof, R.; Bond, W.J.; Stevens, N.; Trollope, W.S.W. Increased tree densities in South African
517 savannas: >50 years of data suggests CO₂ as a driver. *Global Change Biology* **2012**, *18*, 675–684.
518 doi:10.1111/j.1365-2486.2011.02561.x.
- 519 31. Okeke, F.; Karrieli, A. Methods for fuzzy classification and accuracy assessment of historical aerial
520 photographs for vegetation change analyses. Part I: Algorithm development. *International Journal of Remote*
521 *Sensing* **2006**, *27*, 153–176. doi:10.1080/01431160500166540.
- 522 32. Frankl, A.; Seghers, V.; Stal, C.; De Maeyer, P.; Petrie, G.; Nyssen, J. Using image-based modelling
523 (SfM-MVS) to produce a 1935 ortho-mosaic of the Ethiopian highlands. *International Journal of Digital Earth*
524 **2015**, *8*, 421–430. doi:10.1080/17538947.2014.942715.
- 525 33. Ploton, P.; Pélassier, R.; Proisy, C.; Flavenot, T.; Barbier, N.; Rai, S.N.; Couteron, P. Assessing aboveground
526 tropical forest biomass using Google Earth canopy images. *Ecological Applications* **2012**, *22*, 993–1003.
- 527 34. Couteron, P.; Pelissier, R.; Nicolini, E.a.; Paget, D. Predicting tropical forest stand structure parameters
528 from Fourier transform of very high-resolution remotely sensed canopy images. *Journal of Applied Ecology*
529 **2005**, *42*, 1121–1128. doi:10.1111/j.1365-2664.2005.01097.x.
- 530 35. Barbier, N.; Couteron, P.; Proisy, C.; Malhi, Y.; Gastellu-Etchegorry, J.P. The variation of apparent crown
531 size and canopy heterogeneity across lowland Amazonian forests. *Global Ecology and Biogeography* **2010**,
532 *19*, 72–84. doi:10.1111/j.1466-8238.2009.00493.x.
- 533 36. Willcock, S.; Phillips, O.L.; Platts, P.J.; Swetnam, R.D.; Balmford, A.; Burgess, N.D.; Ahrends, A.; Bayliss,
534 J.; Doggart, N.; Doody, K.; Fanning, E.; Green, J.M.H.; Hall, J.; Howell, K.L.; Lovett, J.C.; Marchant, R.;
535 Marshall, A.R.; Mbilinyi, B.; Munishi, P.K.T.; Owen, N.; Topp-Jorgensen, E.J.; Lewis, S.L. Land cover
536 change and carbon emissions over 100 years in an African biodiversity hotspot. *Global Change Biology* **2016**,
537 *22*, 2787–2800. doi:10.1111/gcb.13218.
- 538 37. Lewis, S.L.; Maslin, M.A. Defining the Anthropocene. *Nature* **2015**, *519*, 171–180. doi:10.1038/nature14258.
- 539 38. Bauters, M.; Ampoorter, E.; Huygens, D.; Kearsley, E.; De Hauville, T.; Sellan, G.; Verbeeck, H.; Boeckx,
540 P.; Verheyen, K. Functional identity explains carbon sequestration in a 77-year-old experimental tropical
541 plantation. *Ecosphere* **2015**, *6*, art198. doi:10.1890/ES15-00342.1.
- 542 39. Zuiderweld, K. Contrast Limited Adaptive Histogram Equalization. In *Graphics GEMs IV*; Academic Press:
543 San Diego, CA, USA, 1994; pp. 474–485.
- 544 40. Ullman, S. The Interpretation of Structure from Motion. *Proceedings of the Royal Society of London. Series B,*
545 *Biological Sciences* **1979**, *203*, 405–426.
- 546 41. QGIS Development team., QGIS Geographic Information System., 2018.
- 547 42. Ronneberger, O.; Fischer, P.; Brox, T. U-Net: Convolutional Networks for Biomedical Image Segmentation.
548 In *Medical Image Computing and Computer-Assisted Intervention – MICCAI 2015*; Navab, N.; Hornegger, J.;
549 Wells, W.M.; Frangi, A.F., Eds.; Springer International Publishing: Cham, 2015; Vol. 9351, pp. 234–241.
550 doi:10.1007/978-3-319-24574-4_28.
- 551 43. Chollet, F. *Keras*; GitHub, 2015.
- 552 44. Yakubovskiy, P. *Segmentation Models*; GitHub, 2019.
- 553 45. Martín Abadi.; Ashish Agarwal.; Paul Barham.; Eugene Brevdo.; Zhifeng Chen.; Craig Citro.; Greg S.
554 Corrado.; Andy Davis.; Jeffrey Dean.; Matthieu Devin.; Sanjay Ghemawat.; Ian Goodfellow.; Andrew
555 Harp.; Geoffrey Irving.; Michael Isard.; Jia, Y.; Rafal Jozefowicz.; Lukasz Kaiser.; Manjunath Kudlur.; Josh
556 Levenberg.; Dandelion Mané.; Rajat Monga.; Sherry Moore.; Derek Murray.; Chris Olah.; Mike Schuster.;
557 Jonathon Shlens.; Benoit Steiner.; Ilya Sutskever.; Kunal Talwar.; Paul Tucker.; Vincent Vanhoucke.; Vijay
558 Vasudevan.; Fernanda Viégas.; Oriol Vinyals.; Pete Warden.; Martin Wattenberg.; Martin Wicke.; Yuan Yu.;
559 Xiaoqiang Zheng. *TensorFlow: Large-Scale Machine Learning on Heterogeneous Systems*; 2015.
- 560 46. Buscombe, D.; Ritchie, A. Landscape Classification with Deep Neural Networks. *Geosciences* **2018**, *8*, 244.
561 doi:10.3390/geosciences8070244.

- 562 47. Dale, M.R.T. *Spatial pattern analysis in plant ecology*; Cambridge studies in ecology, Cambridge University
563 Press: Cambridge ; New York, 1999.
- 564 48. Hesselbarth, M.H.K.; Sciajini, M.; With, K.A.; Wiegand, K.; Nowosad, J. landscapemetrics: an open-source
565 R tool to calculate landscape metrics. *Ecography* **2019**.
- 566 49. Bustillo, E.; Raets, L.; Beeckman, H.; Bourland, N.; Rousseau, M.; Hubau, W.; De Mil, T. Evaluation du
567 potentiel énergétique de la biomasse aérienne ligneuse des anciennes plantations de l'INERA Yangambi.
568 Technical report, CIFOR, 2018.
- 569 50. Couteron, P. Quantifying change in patterned semi-arid vegetation by Fourier analysis of digitized aerial
570 photographs. *International Journal of Remote Sensing* **2002**, *23*, 3407–3425. doi:10.1080/01431160110107699.
- 571 51. Hufkens, K. foto: an R implementation of the "fourier transform textural ordination (foto)" method., 2019.
- 572 52. Solórzano, J.V.; Gallardo-cruz, J.A.; González, E.J.; Peralta-carreta, C.; Hernández-gómez, M.; Oca,
573 A.F.m.D.; Cervantes-jiménez, L.G.; Solórzano, J.V.; Gallardo-cruz, J.A.; González, E.J.; Peralta-carreta,
574 C.; Hernández-gómez, M.; Oca, A.F.m.D.; Cervantes-jiménez, L.G. Contrasting the potential of
575 Fourier transformed ordination and gray level co-occurrence matrix textures to model a tropical swamp
576 forest 's structural and diversity attributes. *Journal of Applied Remote Sensing* **2018**, *12*, 036006.
577 doi:10.11117/1.JRS.12.036006.
- 578 53. Kadmon, R.; Harari-Kremer, R. Studying Long-Term Vegetation Dynamics Using Digital
579 Processing of Historical Aerial Photographs. *Remote Sensing of Environment* **1999**, *68*, 164–176.
580 doi:10.1016/S0034-4257(98)00109-6.
- 581 54. Verhoeven, G. BRDF and its Impact on Aerial Archaeological Photography: BRDF and its impact on aerial
582 archaeological photography. *Archaeological Prospection* **2017**, *24*, 133–140. doi:10.1002/arp.1559.
- 583 55. Park, J.Y.; Muller-Landau, H.C.; Lichstein, J.W.; Rifai, S.W.; Dandois, J.P.; Bohlman, S.A. Quantifying Leaf
584 Phenology of Individual Trees and Species in a Tropical Forest Using Unmanned Aerial Vehicle (UAV)
585 Images. *Remote Sensing* **2019**, *11*, 1534. doi:10.3390/rs11131534.
- 586 56. Simini, F.; Anfodillo, T.; Carrer, M.; Banavar, J.R.; Maritan, A. Self-similarity and scaling
587 in forest communities. *Proceedings of the National Academy of Sciences* **2010**, *107*, 7658–7662.
588 doi:10.1073/pnas.1000137107.
- 589 57. Sole, R.V.; Manrubia, S.C. Self-similarity in rain forests: evidence for a critical state. *Physical Review E* **1995**,
590 *51*, 6250 – 6253.
- 591 58. Hughes, M.L.; McDowell, P.F.; Marcus, W.A. Accuracy assessment of georectified aerial photographs:
592 Implications for measuring lateral channel movement in a GIS. *Geomorphology* **2006**, *74*, 1–16.
593 doi:10.1016/j.geomorph.2005.07.001.
- 594 59. Gascon, C.; Williamson, G.B.; Fonseca, G.A.B.d. Receding Forest Edges and Vanishing Reserves. *Science,*
595 *New Series* **2000**, *288*, 1356–1358.
- 596 60. Phillips, O.L.; Rose, S.; Mendoza, A.M.; Vargas, P.N. Resilience of Southwestern Amazon Forests to
597 Anthropogenic Edge Effects. *Conservation Biology* **2006**, *20*, 1698–1710. doi:10.1111/j.1523-1739.2006.00523.x.
- 598 61. Reinmann, A.B.; Hutyra, L.R. Edge effects enhance carbon uptake and its vulnerability to climate
599 change in temperate broadleaf forests. *Proceedings of the National Academy of Sciences* **2017**, *114*, 107–112.
600 doi:10.1073/pnas.1612369114.
- 601 62. Arima, E.Y.; Walker, R.T.; Perz, S.; Souza, C. Explaining the fragmentation in the Brazilian Amazonian
602 forest. *Journal of Land Use Science* **2015**, pp. 1–21. doi:10.1080/1747423X.2015.1027797.
- 603 63. Arima, E.Y.; Barreto, P.; Araújo, E.; Soares-Filho, B. Public policies can reduce tropical deforestation: Lessons
604 and challenges from Brazil. *Land Use Policy* **2014**, *41*, 465–473. doi:10.1016/j.landusepol.2014.06.026.
- 605 64. Larson, A.M. Forest tenure reform in the age of climate change: Lessons for REDD+. *Global Environmental
606 Change* **2011**, *21*, 540–549. doi:10.1016/j.gloenvcha.2010.11.008.
- 607 65. Gourlet-Fleury, S.; Mortier, F.; Fayolle, A.; Baya, F.; Ouédraogo, D.; Bénédet, F.; Picard, N. Tropical forest
608 recovery from logging: a 24 year silvicultural experiment from Central Africa. *Philosophical Transactions of
609 the Royal Society B: Biological Sciences* **2013**, *368*, 20120302. doi:10.1098/rstb.2012.0302.
- 610 66. R Core Team. *R: A Language and Environment for Statistical Computing*; R Foundation for Statistical
611 Computing: Vienna, Austria, 2019.
- 612 67. Hijmans, R.J. *raster: Geographic Data Analysis and Modeling*; 2019.
- 613 68. Leutner, B.; Horning, N.; Schwalb-Willmann, J. *RStoolbox: Tools for Remote Sensing Data Analysis*; 2019.
- 614 69. Wickham, H. *tidyverse: Easily Install and Load the 'Tidyverse'*; 2017.

- 615 70. Arnold, J.B. *ggthemes: Extra Themes, Scales and Geoms for 'ggplot2'*; 2019.
- 616 71. Wickham, H. *scales: Scale Functions for Visualization*; 2018.
- 617 72. Wilke, C.O. *cowplot: Streamlined Plot Theme and Plot Annotations for 'ggplot2'*; 2019.
- 618 73. Pebesma, E. Simple Features for R: Standardized Support for Spatial Vector Data. *The R Journal* **2018**,
- 619 *10*, 439–446. doi:10.32614/RJ-2018-009.
- 620 74. South, A. *rnatuarlearth: World Map Data from Natural Earth*; 2017.

621 © 2019 by the authors. Submitted to *Remote Sens.* for possible open access publication
622 under the terms and conditions of the Creative Commons Attribution (CC BY) license
623 (<http://creativecommons.org/licenses/by/4.0/>).